Structural Basis for α-K Toxin Specificity for K^+ Channels Revealed through the Solution ^{1}H NMR Structures of Two Noxiustoxin−Iberiotoxin Chimeras†

Gilles Ferrat,‡,§ Cedric Bernard,‡,§ Valerie Fremont,|| Theodore J. Mullmann,|| Kathleen M. Giangiacomo,|| and Herve Darbon*,‡

AFMB, CNRS UMR 6098, Chemin Joseph Aiguier, 13402 Marseille Cedex 20, France, and Department of Biochemistry, Temple University School of Medicine, 3420 North Broad Street, Philadelphia, Pennsylvania 19140

Received February 2, 2001; Revised Manuscript Received June 7, 2001

ABSTRACT: Noxiustoxin (NxTX) and iberiotoxin (IbTX) exhibit extraordinary differences in their ability to inhibit current through the large-conductance calcium-activated potassium (maxi-K) and voltage-gated potassium (Kv1.3) channels. The three-dimensional structures of NxTX and IbTX display differences in their α/β turn and in the length of the α-carbon backbone. To understand the role of these differences in defining specificity, we constructed two NxTX mutants, NxTX−IbTX I and NxTX−IbTX II, and solved their solution structures by ^{1}H NMR spectroscopy. For NxTX−IbTX I, seven amino acids comprising the α/β turn in NxTX are replaced with six amino acids from the corresponding α/β turn in IbTX (NxTX-YGSSAGA$_{21-27}$FGVDRF$_{21-26}$). In addition, NxTX−IbTX II contained the S14W mutation and deletion of the N- and C-terminal residues. Both NxTX−IbTX I and NxTX−IbTX II exhibit an α/β scaffold structure typical of the α-K channel toxins. A helix is present from residues 10 to 19 in NxTX−IbTX I and from residues 13 to 19 in NxTX−IbTX II. The β-sheet, defined by three antiparallel strands, is one residue longer in NxTX−IbTX I relative to NxTX−IbTX II. The two toxins also differ in the structure of the α/β turn with NxTX−IbTX I resembling that of IbTX and with NxTX−IbTX II resembling that of NxTX. These differences in the β-sheet and α/β turn alter the dimensions of the toxin−channel interaction surface and provide insight into how these NxTX mutations alter K^+ channel specificity for the maxi-K and Kv1.3 channels.

The α-K channel toxin (α-KTx)[1] peptides, from scorpion venoms, represent a family of small, highly basic peptides that inhibit the flow of potassium ions through potassium channels by binding to and occluding the extracellular pore of the channel (*1*−*3*). The α-KTx peptides can be grouped into three subfamilies (α-KTx 1.x, α-KTx 2.x, and α-KTx 3.x) on the basis of differences in their amino acid sequences (*4*, *5*). These subfamilies display remarkable differences in their specificity for voltage-gated potassium (Kv) and large-conductance, calcium-activated potassium (maxi-K) channels. In particular, iberiotoxin (IbTX or α-KTx 1.3) is highly specific for the maxi-K channel and does not inhibit Kv channels with high affinity (*6*, *7*). In contrast, noxiustoxin (NxTX or α-KTx 2.1), which inhibits some Kv channels with high affinity (*8*), displays an extraordinary ability to discriminate against the maxi-K channel (*9*). Because these α-KTx peptides bind to the potassium channel pore, the determinants for binding specificity may provide insight into differences in the architecture of the Kv and maxi-K channel vestibules.

The three-dimensional structures of the α-KTx peptides, determined by ^{1}H NMR spectroscopy, may disclose structural elements that control binding specificity. The structures for α-KTx peptides from the three subfamilies, α-KTx 1.x (*10*, *11*), α-KTx 2.x (*12*, *13*), and α-KTx 3.x (*14*, *15*), have been solved. All display a α/β motif with a β-sheet formed from two or three antiparallel strands on one face of the molecule and an α-helix on the other. The helix and sheet form a compact structure held together by two of the three disulfide bonds. Thus, the overall tertiary structure of the α-KTx peptides is similar. However, the α-KTx subfamilies show differences in the length of their α-carbon backbone and in the α/β turn that may underlie their observed specificity.

To understand how these differences in the α-carbon backbone alter the toxin binding surface, we constructed two NxTX mutants (NxTX−IbTX I and NxTX−IbTX II). Each of these mutants was altered in the length of the α-carbon backbone and in the α/β turn relative to NxTX (Table 1). For both mutants, seven amino acids comprising the α/β turn in NxTX (YGSSAGA$_{21-27}$) were replaced with six structurally equivalent residues from IbTX (FGVDRG$_{21-26}$). In addition to this mutation, NxTX−IbTX II includes deletion

† This work was supported in part by NIH Grant GM52179 and in part by la Fondation pour la Recherche Médicale.

* Corresponding author. E-mail: herve@afmb.cnrs-mrs.fr. Tel: 33 491 16 45 35. Fax: 33 491 16 45 36.

‡ AFMB, CNRS UMR 6098, Chemin Joseph Aiguier.

§ G.F. and C.B. have contributed equally to this work.

|| Temple University School of Medicine.

[1] Abbreviations: α-KTx, α-K channel toxin; α-KTx 1.1, charybdotoxin; α-KTx 1.3, iberiotoxin; α-KTx 2.1, noxiustoxin; α-KTx 3.2, agitoxin 2; AgTX2, agitoxin2; ChTX, charybdotoxin; DQF-COSY, double-quantum-filtered two-dimensional correlation spectra; IbTX, iberiotoxin; Kv channel, voltage-gated potassium channel; maxi-K channel, large-conductance calcium-activated potassium channel; NOE, nuclear Overhauser effect; NOESY, phase-sensitive two-dimensional nuclear Overhauser effect spectra; NxTX, noxiustoxin; TOCSY, clean total correlation spectra.

10.1021/bi010228e CCC: $20.00
Published on Web 08/24/2001

Table 1: Amino Acid Sequence Alignment of IbTX, NxTX, NxTX−IbTX I, and NxTX−IbTX II

	1 5 10 15 20 25 30 35 37
IbTX	**ZFTDVDCSVSKECWSVCKDLFGV-DRGKCMGKKCRCYQ**
NxTX	TIINVKCTSPKQCSKPCKELYGSSAGAKCMNGKCKCYNN
NxTX-IbTX I	TIINVKCTSPKQCSKPCKEL**FGV-DRG**KCMNGKCKCYNN
NxTX-IbTX II	-IINVKCTSPKQC**W**KPCKEL**FGV-DRG**KCMNGKCKCYN**-**

of T1 and N38 and the site-directed mutation, S14W. The latter S14W mutation incorporates a residue that is critical for a high-affinity interaction with the maxi-K channel (*16*). Functional studies reveal that the interactions of NxTX−IbTX I and NxTX−IbTX II display opposing changes in their binding specificity for maxi-K and Kv1.3 channels (*9*). For the maxi-K channel, NxTX−IbTX I and NxTX−IbTX II both display measurable binding interactions, in the nanomolar to micromolar range, while NxTX does not. Conversely, for the Kv1.3 channel, the two mutants display a significantly weaker interaction relative to recombinant NxTX (NxTX−IbTX I, 60-fold; NxTX−IbTX II, 1500-fold).

To understand the structural basis for these changes in binding specificity, we examined the solution structures of NxTX−IbTX I and NxTX−IbTX II by ^{1}H NMR spectroscopy. The structures obtained differ in the length of the β-sheet face and in the α/β turn. Together, these differences in the backbone conformation alter the shape of the toxin binding surface. These structural studies are consistent with functional studies and suggest that the maxi-K channel is exquisitely sensitive to the dimensions of the toxin β-sheet face compared to the Kv1.3 channel (*9*). Thus, the backbone of the α-KTX peptides presents an extraordinarily sensitive way for altering toxin−channel specificity.

MATERIALS AND METHODS

Expression and Purification of Recombinant NxTX−IbTX Peptides. NxTX−IbTX I and NxTX−IbTX II were expressed and purified as described previously (*9*). The identity of the purified peptides used for ^{1}H NMR spectra was confirmed by MALDI-MS mass spectrometric analysis (Protein Chemistry Laboratory, University of Pennsylvania).

Sample Preparation. NxTX−IbTX I (2.5 mg) and NxTX−IbTX II (7.5 mg) were dissolved in 0.5 mL of H_2O/D_2O (90/10 v/v), pH = 3, uncorrected for isotope effects, leading to concentrations of 1.2 and 3.6 mM, respectively.

NMR Spectroscopy. Proton 2D NMR spectra were first routinely recorded at 283 and 300 K in order to solve assignment ambiguities. All of the data were collected on a Bruker DRX 500. Double-quantum-filtered two-dimensional correlation spectra (DQF-COSY) (*17*) were acquired in the phase-sensitive mode by time-proportional phase incrementation of the first pulse (TPPI) (*18*). Clean total correlation spectra (TOCSY) (*19*, *20*) were acquired with a spin lock of 80 ms. Phase-sensitive two-dimensional nuclear Overhauser effect (NOE) spectra (NOESY) (*21*, *22*) with watergate (*23*) composite were acquired using the TPPI method with mixing times from 80 to 150 ms. The solvent-OH resonance was suppressed either by low-power irradiation during the relaxation delay or, for NOESY spectra, during the mixing time or by using a watergate 3-9-19 pulse train (*23*) using a gradient at the magic angle obtained by applying simultaneously *x*-, *y*-, and *z*-gradients prior to detection.

For determination of amide proton exchange rates, the peptide was lyophilized twice and solubilized in 100% D_2O. Immediately after solubilization, a series of NOESY spectra with mixing times of 80 ms were recorded at 283 K, the first one during a time period of 1 h (1024 complex points with 256 experiments), followed by spectra of 10 h (1024 complex points with 512 experiments).

Data Processing. All of the data were processed using the Bruker software XWINNMR running on a Silicon Graphic INDY R4000 workstation. The matrices were transformed with a zero filling to the next power of two in the acquisition dimension and to 1024 points in the other. The signal was multiplied by a shifted sine-bell window in both dimensions prior to Fourier transform, and a fifth-order polynomial baseline correction was applied. Spectra had finally a 12 ppm width with a digital resolution of 2.93 Hz/point in the ω_2 dimension and 5.85 Hz/point in the ω_1 dimension.

Spectral Analysis. The spectral analyses were performed using the XEASY software (*24*) running on a Silicon Graphic R10000 workstation. The identification of amino acid spin systems and the sequential assignment were performed using the standard strategy described by Wüthrich (*25*). The comparative analysis of COSY and TOCSY spectra recorded in water gave the spin system signature of the protein. The spin systems were sequentially connected using the NOESY spectra.

Experimental Restraints. The integration of NOE data using manual integration in the XEASY software permitted us to obtain volumes and to convert them into distance restraints using the CALIBA routine of the DIANA package, according to calculated curves, function of $1/r^6$ for intraresidual and sequential NOE involving HN, Hα, and Hβ, as well as medium- and long-range NOE involving backbone protons, and function of $1/r^4$ for others. We thus obtained a set of restraints with upper limits defined for each volume. The ϕ torsion angle constraints resulted from the $^3J_{HN\alpha}$ coupling constant measurements obtained by INFIT routine from XEASY software. For a given residue, separated NOESY cross-peaks with the backbone amide proton in the ω_2 dimension were used. Several cross sections through these cross-peaks were selected that exhibited a good signal to noise ratio. They were added up, and only those data points of the peak region that were above the noise level were retained. The left and the right ends of the peak region were then brought to zero intensity by a linear baseline correction. After extending the baseline-corrected peak region with zeros on both sides, which is equivalent to oversampling in the time domain, an inverse Fourier transformation was performed. The value of the $^3J_{HN\alpha}$ coupling constant was obtained from the first local minimum. The constants were then divided into small (<7 Hz) and large (>7.5 Hz) and translated into −40°/−70° and −70°/−170° angle restraints,

respectively. The stereospecific assignment was made using the HABAS routine of the DIANA software (*26*, *27*) on the basis of the upper limit restraints and $^3J_{HN\alpha}$, $^3J_{H\alpha H\beta 2}$, and $^3J_{H\alpha H\beta 3}$. Pseudoatom corrections were applied by DIANA when stereospecific assignments could not be obtained.

Structure Calculations. Distance geometry calculations were performed with the variable target function program DIANA 2.8. A preliminary set of 1000 structures was initiated including only intraresidual and sequential upper limit distances. From these, the 500 best were kept for a second round, including medium-range distances, and the resulting 250 best for a third one, with the whole set of upper limit restraints, and some additional restraints, used to define the disulfide bridges (i.e., dSγ/Sγ, 2.1 Å; dCβ/Sγ, 3.1 Å). Starting from the 100 best structures, according to their target function, a REDAC (*27*) strategy was used in the last step in order to include the dihedral constraints together with the additional distance restraints coming out from hydrogen bonds.

The 25 structures exhibiting the lowest target function were then energy-minimized over 2500 iterations of the Powell algorithm of the X-PLOR 3.1 (*28*) package using the CHARMM force field (parameter files parmallh6x.pro and topallh3x.pro).

The visual analysis of the resulting structures was carried out with TURBO (*29*) graphic software as well as with MOLMOL (*30*) software. RSMD data were obtained by MOLMOL software. The quality of the structures was analyzed using PROCHECK-NMR (*31*) software.

Electrostatic Calculations. The electrostatic potential throughout the volume of the toxin and toxin dipole moments together were calculated using GRASP (*32*) as described (*33*). The electrostatic potential maps were calculated using two different charge sets. One includes only ionizable groups at the N- and C-termini and on arginine, lysine, aspartate, and glutamate. The second set assigns partial charges to all ionizable groups and to atoms in the α-carbon backbone.

RESULTS

Sequential Assignment. Both NxTX−IbTX peptides were sequentially assigned following the standard method of Wüthrich (*25*). Below is the description of the sequential assignment for NxTX−IbTX II. For NxTX−IbTX I, the same pattern has been obtained except for the N-terminus where the spin system lacking the amide proton frequency was a threonine instead of an isoleucine. The spin systems were identified on the basis of both COSY and TOCSY spectra recorded in water at 300 and 283 K. The use of two temperatures for recording allowed us to resolve overlapping signals in the fingerprint region, leading to complete assignment of intraresidue HN-Hα cross-peaks. Starting from them, each spin system was characterized by its connectivities in the COSY and checked in the TOCSY spectra. Few methyl groups have only one chemical shift frequency, due to their strict degeneracy or uncertainty in overcrowded regions. The sequential connectivities were obtained from NOESY spectra, recorded in water at both 300 and 283 K, with a mixing time of 80 ms. The Hα-HN, HN-HN pathways are illustrated in Figure 1. The NxTX−IbTX II peptide contained only one leucine, one threonine, and one serine. Those spin systems were unambiguously attributed: leucine 19, threonine 7, and

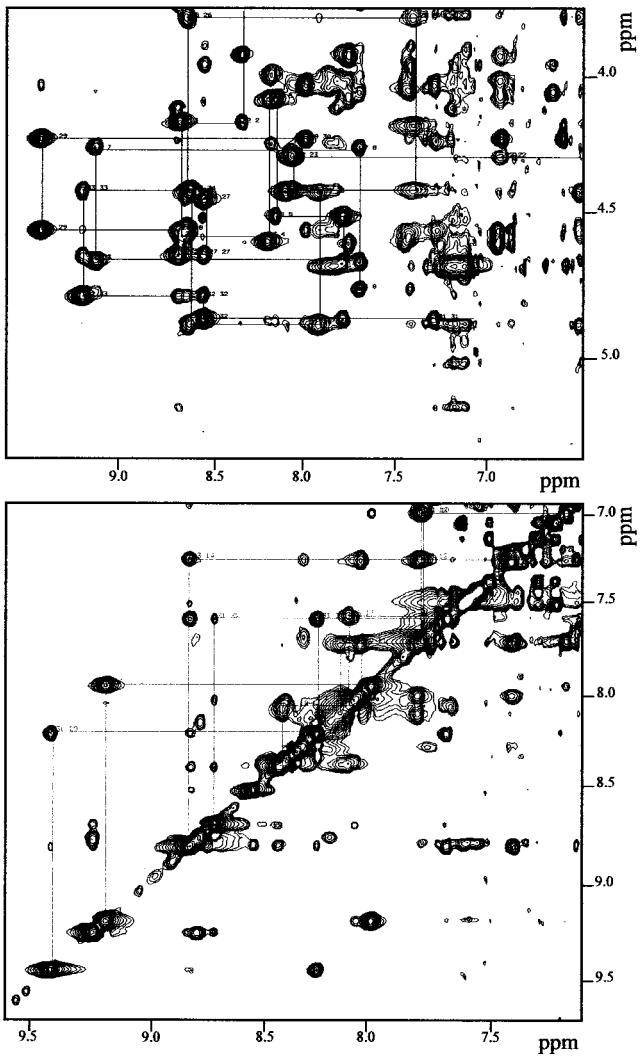

FIGURE 1: Contour plots of a NOESY spectrum recorded on NxTX−IbTX I peptide. Top: Fingerprint region. Bottom: Amide proton region. Some sequential connectivities are illustrated by lines.

serine 8. The discrimination of the two isoleucines of the molecule was done assuming the isoleucine 1 NH_2 group is in fast exchange with water and therefore lacks the TOCSY tower on the HN frequency. Conversely, the one which produced a TOCSY tower on the HN frequency was assigned as isoleucine 2. These assigned spin systems were used to assign the rest of the spin systems by sequentially connecting them by virtue of sequential Hα-HN for the extended structures or HN-HN for the helical structures. These connections are confirmed by Hβ-HN or Hγ-HN connectivities. These results are summarized in Figure 2.

Additional Restraints. We measured 27 $^3J_{HN\alpha}$ coupling constants on NOESY spectra of NxTX−IbTX II by using the INFIT software. The missing constants correspond to the three glycines, the two prolines, the isoleucine 1, the phenylalanine 20, the lysine 31, and the asparagine 36, for which INFIT did not succeed in determining $^3J_{HN}$ coupling constants.

A total of 20 $^3J_{\alpha\beta}$ constants for NxTX−IbTX II were obtained from the COSY spectra (digital resolution 0.73 Hz/point), compared with simulated signals. β protons of asparagine 3, cysteine 12, and serine 8 were stereospecifically assigned. We measured the exchange rate of amide protons with the solvent. The amide protons still giving rise to NOE

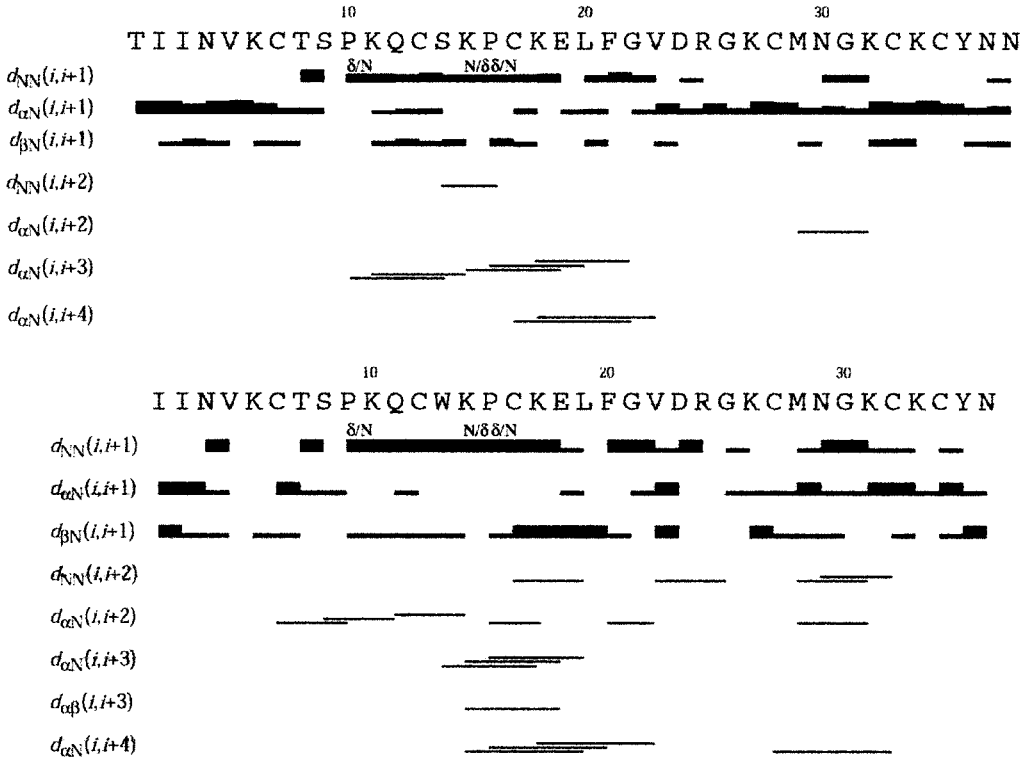

FIGURE 2: Sequence-specific assignments of NxTX−IbTX I (top) and NxTX−IbTX II (bottom) from NOE data. Collected sequential NOE's are classified into strong and weak NOE's and are indicated by thick and thin bars, respectively. The medium-range NOE's are indicated without mention of their intensity.

Table 2: Structural Data from the 25 Best Structures of NxTX−IbTX I and NxTX−IbTX II

	NxTX−IbTX I	NxTX−IbTX II
RMSD (Å)		
backbone (C, Cα, N)	0.96 (±0.23)	0.85 (±0.23)
all heavy atoms	1.90 (±0.23)	1.75 (±0.23)
energy (kcal/mol)		
total	−219.57	−134.04
bonds	0.57	11.82
van der Waals	−220.68	−165.67
dihedral	0.78	1.33
NOE	0.78	0.10

cross-peaks after 50 h of exchange were considered as being engaged in hydrogen bonds. Most of them occurred in the regular structures, such as HN of C6, Q11, C12, W13, and C16 in the α-helix and of V22, K26, M28, G30, K31, C32, and K33 in the β-sheet. The partner of the C6 HN has been identified as the V4 CO group.

Structure Calculations. For NxTX−IbTX II (NxTX−IbTX I), the whole set of constraints included 433 (346) distance restraints extracted from NOE's 119 (117) intraresidues, 132 (110) sequential, 90 (27) medium-range, and 59 (37) long-range restraints, 33 restraints taken out from hydrogen-exchange analysis and 24 angle restraints extracted from coupling constant measurements [i.e., an average of 12.7 (11.2) restraints/residue; see Table 2]. The distance geometry calculations using this whole set of restraints led to a single family of 25 structures for NxTX−IbTX I and NxTX−IbTX II; see Figure 3a. These 25 structures are all consistent with the experimental restraints, and none of them present NOE violations larger than 0.2 Å. Furthermore, no residual unassigned NOE cross-peaks were present at the end of the calculation process.

These 25 structures, having some important nonbonded bad contacts, have been energy minimized with the Powell algorithm of the X-PLOR 3.1 software. In the resulting final structures, the negative van der Waals energy indicates the absence of nonbonded contacts (Table 2). The covalent geometry is respected as indicated by the low RMSD values on the bond lengths and the valence angles. No NOE violation larger than 0.15 Å was detected. The RMSD of these 25 structures are 0.85 Å for the backbone atoms and 1.75 Å for all of the heavy atoms (according to the MOLMOL software, Figure 3a). The overall backbone geometry is in agreement with predicted torsion angles. Ramachandran analysis (not shown) revealed 61.2% of the residues in the most favored regions, 38.5% in additional and generously additional regions, and 0.3% in disallowed regions, according to the PROCHECK-NMR software nomenclature.

Structure Description of NxTX−IbTX I and NxTX−IbTX II. The calculated structures of NxTX−IbTX II and NxTX−IbTX I share the same fold which is characteristic of the α-KTx family of peptides. The RMSD values of the 25 structures allow us to describe the classic α/β scaffold: a three-stranded β-sheet and an α-helix (Figure 3b). The precise location of these secondary structures has been done by PROCHECK-NMR, which indicates the presence of an α-helix running from residues 10 to 19 (two turns and a half of helix) for NxTX−IbTX II and from residues 13 to 19 for NxTX−IbTX I. In addition, the β-sheet is made of stretches 2−3, 25−28, and 31−34 for NxTX−IbTX II and 2−3, 24−29, and 32−36 for NxTX−IbTX I. The 2−3 stretch is nonclassical since it is only two residues long and situated at the N-terminus of the molecule. The second and the third strands are connected by an undefined β-turn formed by

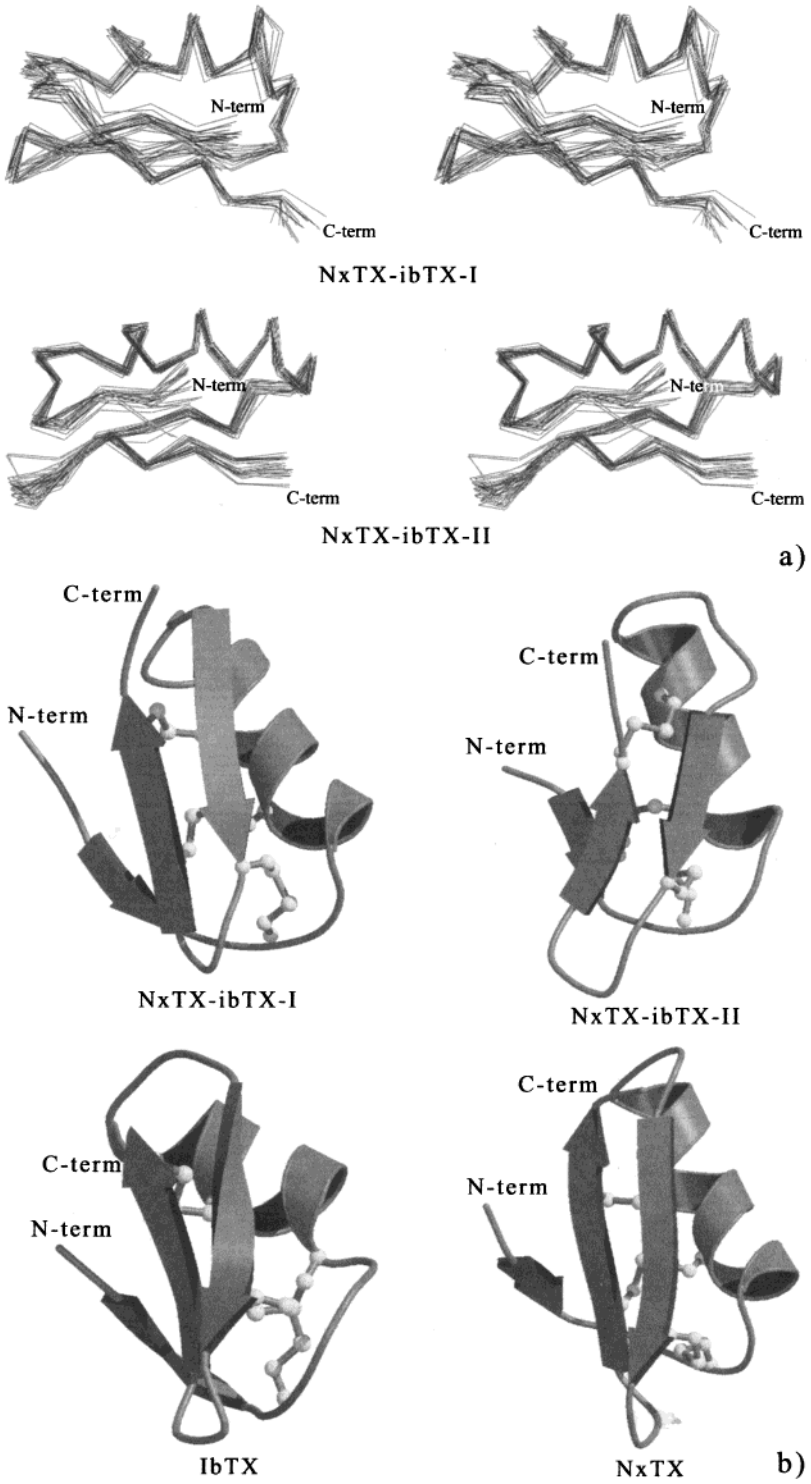

FIGURE 3: (a) Stereoview of the 25 best structures for NxTX−IbTX I (top) and NxTX−IbTX II (bottom). Only the Cα traces are displayed. (b) Molscript diagrams showing the secondary structures for NxTX−IbTX I, NxTX−IbTX II, IbTX, and NxTX.

residues N29 and G30 for NxTX−IbTX II and N30 and G31 for NxTX−IbTX I. The high RMSD of this region shows that this part of the peptide is flexible, as in the original NxTX (*12*). Despite the presence of *i*,*i*+2 correlations between the amide protons of residues 28−30 and 29−31 and the hydrogen bond between the carbonyl of the M28 and the amide proton of K31, it has been impossible to classify this turn. These secondary structures for NxTX−IbTX I and NxTX−IbTX II are in full accordance with the experimental data.

Electrostatic Features of NxTX−IbTX I and NxTX−IbTX II. The α-KTx peptides are highly charged peptides, and these charges have been shown to have profound effects on their interactions with the extracellular vestibules of K channels (*33*−*35*). Similar to NxTX, NxTX−IbTX I and NxTX−IbTX II both have a large net positive charge of 6. However, the total number of ionizable charges in these NxTX−IbTX (+9, −3) chimeras is greater than in NxTX (+8, −2). The extra ionizable residues in the chimeras derive from the presence of an Asp and Arg in the α/β turn (Table

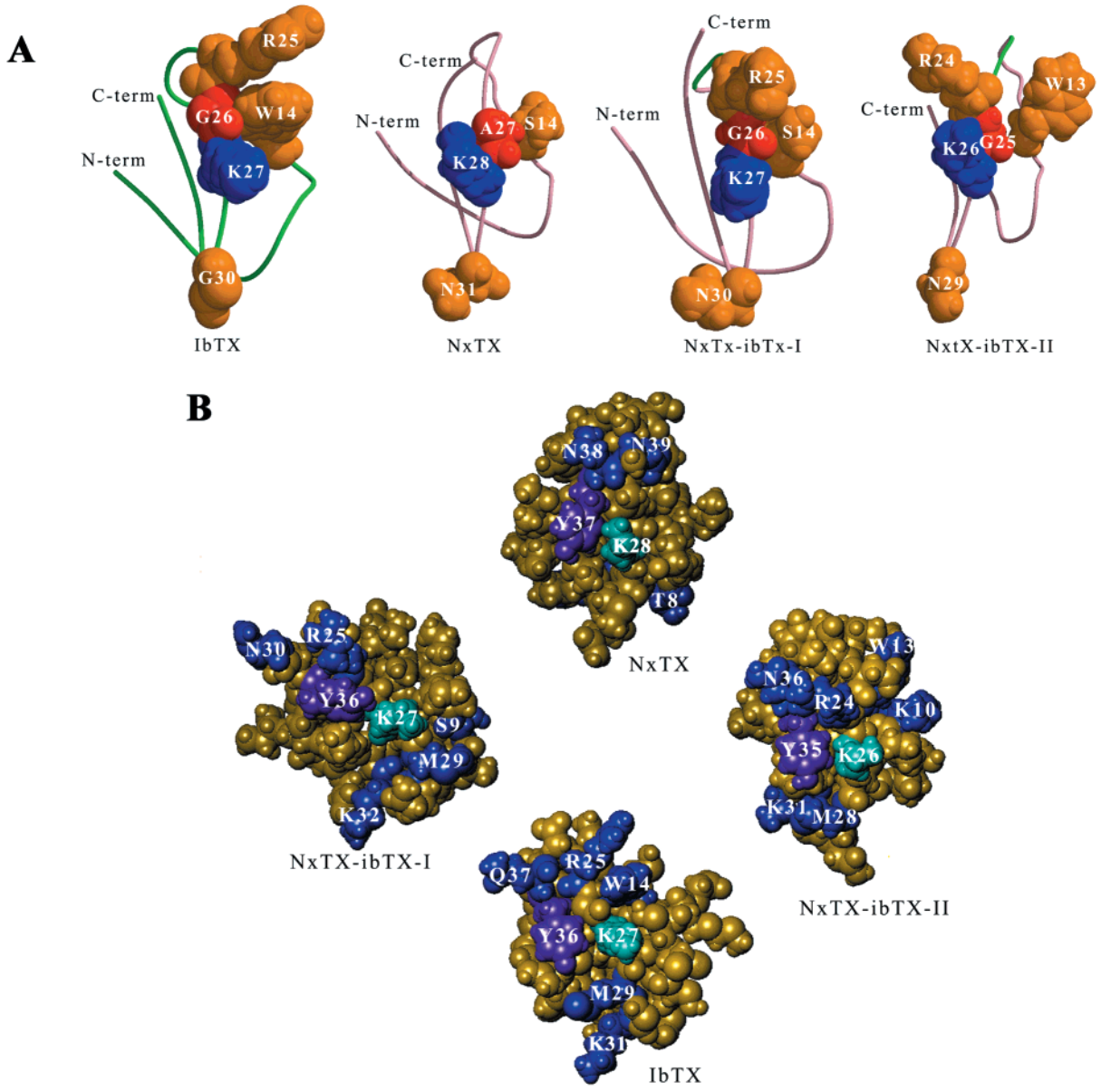

FIGURE 4: Comparison of NxTX−IbTX chimera structures to NxTX and IbTX. (A) Molscript diagrams of structures for NxTX−IbTX I, NxTX−IbTX II, NxTX, and IbTX. Key residues are in CPK representation. Lys27, colored blue, interacts with a K^+ binding site in the maxi-K channel pore (*33*, *35*). Arg25 and Trp14, colored yellow, are uniquely critical for a high-affinity interaction with the maxi-K channel (*16*). Residues in the β-turn, colored yellow, form an important part of the toxin−K channel interaction surface (*2*, *16*, *36*). Gly26, colored red, in IbTX (α-KTx 1.3) is reported to define the orientation of the helix and sheet in the α-KTx 1.x subfamily (*41*). The structural equivalent of this residue in NxTX is Ala27. Structurally equivalent residues in NxTX−IbTX I and NxTX−IbTX II are similarly color coded. (B) CPK representation of the interaction surface of IbTX, NxTX, NxTX−IbTX I, and NxTX−IbTX II. The residues involved in the binding of the toxins are in blue for all but the critical lysine (in light blue) and the aromatic residue (in purple).

1). To understand how these extra charges influence their electrostatic structures, we calculated the dipole moments and electrostatic potential around the NxTX−IbTX molecules. The calculated dipole moments for NxTX−IbTX I (87 D) and NxTX−IbTX II (66 D) are slightly larger than that for NxTX (55 D). However, the relative orientations of the dipole moments for both chimeras (Figure 5) are similar to that of NxTX. Figure 5 also shows the positive (turquoise) and negative (magenta) isopotential surfaces at 2 kT overlaying the α-carbon backbones for NxTX−IbTX I (parts A and B) and NxTX−IbTX II (parts C and D). Consistent with the large net positive charge, the positive isopotential surfaces enclose a much larger volume than the negative isopotential surfaces. At low ionic strength, parts A and C of Figure 5, the positive isopotential surfaces enclose a large volume, ~39 000 Å^3. Indeed, these surfaces extend far (~10 Å) beyond the molecular surface (not shown). In contrast, at high ionic strength (150 mM), parts B and D of Figure 5, the positive isopotential surfaces enclose a much smaller volume, ~4000 Å^3. This large change in volume with ionic strength is consistent with the finding that the association rate constants for NxTX−IbTX II are exquisitely sensitive to external ionic strength (*9*).

DISCUSSION

Comparison of NxTX−IbTX I and NxTX−IbTX II to Related Toxins. NxTX−IbTX I and NxTX−IbTX II adopt the classical scorpion toxin α/β scaffold (Csα/β motif), which has been described as a α-helix covalently linked through two disulfide bridges to an antiparallel β-sheet. This motif

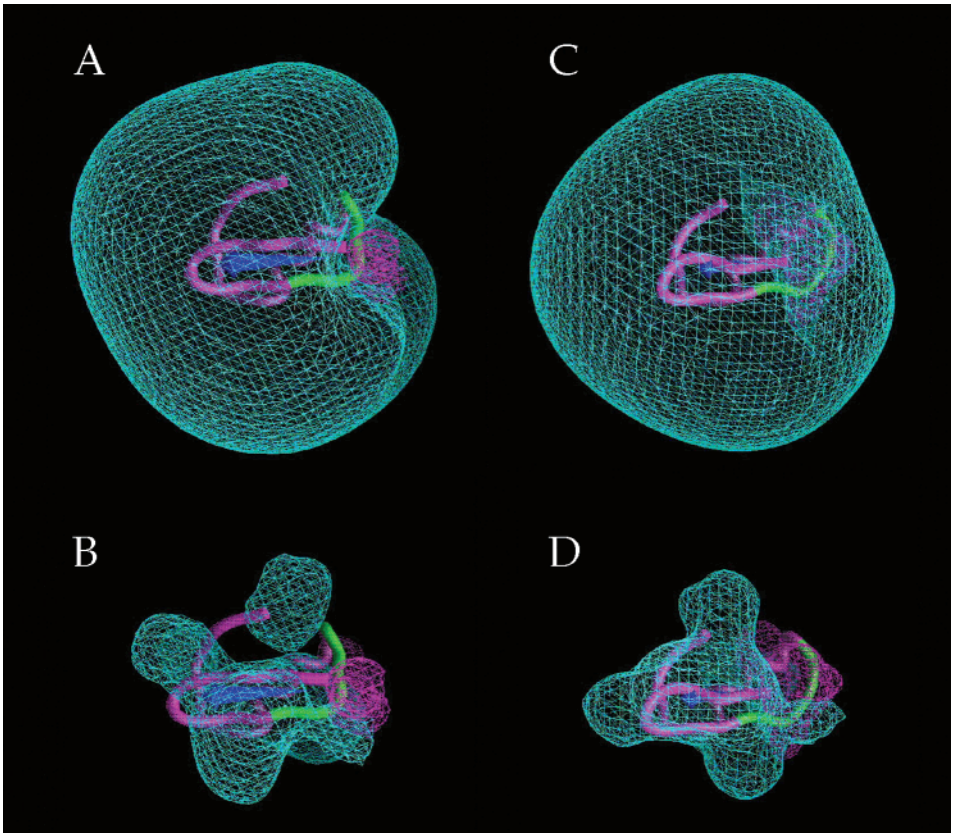

FIGURE 5: Isopotential energy surfaces for NxTX−IbTX I and NxTX−IbTX II. Parts A and C show the isopotential energy surfaces at +2 kT (turquoise) and −2 kT (magenta) calculated with 0 mM ionic strength for NxTX−IbTX I and NxTX−IbTX II, respectively. Parts B and D show the isopotential energy surfaces at +2 kT (turquoise) and −2 kT (magenta) calculated with 150 mM ionic strength for NxTX−IbTX I and NxTX−IbTX II, respectively. The orientation and relative magnitudes of the calculated dipole moments for NxTX−IbTX I (87 D) and NxTX−IbTX II (66 D) are shown in blue. Electrostatic calculations for the structures shown were done using GRASP (*32*) with a charge set that includes only the ionizable residues, see Materials and Methods. For both chimeras, the α-carbon backbone residues from NxTX are shown in magenta while those from IbTX are shown in green.

is characteristic of all α-KTx toxin subfamilies. The overall structures of NxTX−IbTX I and NxTX−IbTX II are very similar to those of NxTX (α-KTx 2.1) and IbTX (α-KTx 1.3) (Figure 4). However, there are important differences in the secondary and tertiary structures of these toxins that are likely to differently influence their binding interactions with maxi-K and Kv channels.

A substantial body of data supports the fact that the α-KTx β-sheet face forms its binding surface with the potassium channel external vestibule. For both NxTX−IbTX peptides, the reverse turns between the second and third antiparallel β-strands are similar to that of NxTX. As in NxTX, this turn is flexible compared to IbTX. This difference in flexibility may derive from the fact that in NxTX and the NxTX−IbTX peptides this turn includes an asparagine followed by a glycine. However, in IbTX and all α-KTx 1.x peptides, this turn consists of either a glycine or asparagine followed by a lysine. The presence of this lysine is likely to restrict the flexibility of this turn. Additionally, in AgTX2 (α-KTx 3.2) an arginine at this position was found to interact with a specific residue in the Shaker Kv channel (*36*). The residues in this turn are also critical for a high-affinity interaction with the maxi-K channel (*16*). Thus, the identities of residues in this reverse turn are important determinants of α-KTx binding to the maxi-K and Kv channels.

The length of the antiparallel β-strands may also be an important determinant of α-KTx binding specificity. NxTX (α-KTx 2.1) contains two extra amino acids compared to IbTX (α-KTx 1.3), 39 vs 37, which increase the length of the first and third antiparallel strands of the β-sheet face in NxTX (*4*, *12*). The NxTX−IbTX peptides are both reduced in length compared to NxTX because seven residues comprising the α/β turn in NxTX are replaced with six structurally equivalent residues in IbTX. Thus, NxTX−IbTX I, which contains only this mutation, is 38 residues in length. With additional amino acid deletions at both the N- and C-termini, NxTX−IbTX II is 36 residues in length. From the solution structures it is clear that the third antiparallel strand in NxTX−IbTX II is decreased in length compared to NxTX−IbTX I (Figure 3). Interestingly, NxTX−IbTX I shows an ∼15-fold weaker interaction for the maxi-K channel compared to NxTX−IbTX II and NxTX−IbTX III mutants, which both contain this C-terminal deletion (*9*). Thus, this increased length of the third antiparallel β-strand in NxTX−IbTX I could contribute to its relatively weak interaction with the maxi-K channel.

Intriguingly, peptides from the α-KTx 3.x subfamily (*4*, *15*) also display an increased length of the third antiparallel strand compared to the α-KTx 1.x subfamily of peptides. Peptides from this subfamily do not block the maxi-K channel with high affinity (*37*). Thus, the extra length of the β-sheet face may be a defining feature in maxi-K channel discrimination of the α-KTx 2.x and α-KTx 3.x subfamilies.

NxTX and IbTX also display differences in the packing of their helix and sheet, as can be seen from Figure 3b. For NxTx the plane of the β-sheet face and long axis of the helix

are roughly parallel. In contrast, for IbTx, the β-sheet face plane and helix axis are tilted by roughly 45°. Analysis of the solvent-accessible residues in charybdotoxin (ChTX or α-KTx 1.1) suggested that the packing of the helix and sheet should be critically dependent upon a highly conserved glycine that is not solvent accessible (*38*). In the α-KTx 1.x and α-KTx 3.x subfamilies, this "Gly26" is strictly conserved. However, in NxTX this position is occupied by an alanine. Both NxTX−IbTX peptides contain the critical Gly26. Thus, we expected both of these peptides to resemble IbTX in their packing of the helix and sheet. Surprisingly, these peptides differ in the packing of their helices and sheets (Figure 3b). For NxTX−IbTX I, the β-sheet plane and helix are roughly parallel, as seen for IbTX. Conversely, NxTX−IbTX II resembles NxTX in that the β-sheet plane and helix are tilted by roughly 45°. Our results suggest that, in addition to the culprit Gly26, other structural features help to define the packing of the helix and sheet in the α-KTx peptides.

These differences in the orientation of the β-sheet plane and helix correlated with differences in the α/β turn. The α/β turn in NxTX−IbTX I resembles that in IbTX while the α/β turn in NxTX−IbTX II resembles that in NxTX. These differences in the α/β turn and in packing of the helix and the sheet alter the geometry of the toxin binding surface. The importance of this altered toxin binding surface can be understood by examining the location of toxin residues critical to a high-affinity interaction with the maxi-K channel (Figure 4). Mutagenic work with charybdotoxin (ChTX or α-KTx 1.1) showed that eight residues, protruding from the β-sheet face, were critical for a high-affinity interaction with the maxi-K channel. Moreover, two of these residues, R25 and W14, are uniquely conserved in the α-KTx 1.x subfamily. NxTX−IbTX II contains six of the eight critical residues including R25 and W14 (*16*). However, the interaction of the maxi-K channel with NxTX−IbTX II is >1000-fold weaker than its interaction with either ChTX (α-KTx 1.1) (*39*) or IbTX (α-KTx 1.3) (*1*). Figure 4 shows that the relative positions of R25 and W14 in NxTX−IbTX II differ from those in IbTX (α-KTx 1.3). Thus, the optimal interaction of these toxin residues with channel residues may be disrupted. In addition, the altered location of these and other residues may introduce new unfavorable interactions with the maxi-K channel vestibule. These functional (*9*) and structural results suggest that the α-carbon backbone provides an extraordinarily sensitive way for altering α-KTx molecular recognition of K channels through subtle rearrangement of the functional surface involved in the interaction of toxins with the K channels (Figure 4B).

The NxTX−IbTX structures solved in this work in combination with functional studies (*9*) suggest that the α/β turn and the length of the β-sheet face may help to define the α-KTx discrimination of maxi-K and Kv channels. Therefore, it is natural to ask, what can these molecular differences tell us about the architecture of maxi-K and Kv channels? The minimal functional unit of a K channel is a homotetramer of subunits symmetrically arranged around a central aqueous pore (*40*). Thermodynamic mutant cycle analysis with AgTX2 (α-KTx 3.2) and the Shaker Kv channel showed that two different toxin residues at either end of the β-sheet face (i.e., the reverse turn and α/β turn) interact with identical channel residues on diametrically opposed subunits (*36*). As a rigid molecular caliper, the dimensions of the toxin β-sheet face may provide insight into the molecular architecture of the K channel vestibules. In this regard, the exquisite sensitivity of the maxi-K channel to the length of the β-sheet face, compared to Kv channels (*9*), hints at fundamental differences in their external vestibules. Indeed, docking NxTX and IbTX into a three-dimensional model of the maxi-K channel vestibule revealed that the extra length of the β-sheet face in NxTX creates a sterically unfavorable interaction with residues in diametrically opposed subunits (Dr. Ying Duo-Gao, Merck Research Laboratories, personal communication). Thus, by exploring α-KTx peptides of extraordinarily different patterns of specificity, this work points to a new way for probing molecular differences in the architectures of K channel vestibules.

ACKNOWLEDGMENT

We thank Dr. Ying-Duo Gao (Merck Research Laboratories) for sharing structural models of the maxi-K and Kv channel vestibules with us and for valuable discussions on them. We thank Dr. Maria Garcia (Merck Research Laboratories) for helpful comments on the manuscript and beneficial discussions on K channel vestibules.

REFERENCES

1. Giangiacomo, K. M., Garcia, M. L., and McManus, O. B. (1992) *Biochemistry 31*, 6719−6727.
2. Goldstein, S. A., Pheasant, D. J., and Miller, C. (1994) *Neuron 12*, 1377−1388.
3. MacKinnon, R., and Miller, C. (1988) *J. Gen. Physiol. 91*, 335−349.
4. Giangiacomo, K. M., Gabriel, J., Fremont, V., and Mullmann, T. J. (1999) *Perspect. Drug Discovery Des. 15/16*, 167−186.
5. Miller, C. (1995) *Neuron 15*, 5−10.
6. Galvez, A., Gimenez-Gallego, G., Reuben, J. P., Roy-Contancin, L., Feigenbaum, P., Kaczorowski, G. J., and Garcia, M. L. (1990) *J. Biol. Chem. 265*, 11083−11090.
7. Koschak, A., Koch, R. O., Liu, J., Kaczorowski, G. J., Reinhart, P. H., Garcia, M. L., and Knaus, H. G. (1997) *Biochemistry 36*, 1943−1952.
8. Grissmer, S., Nguyen, A. N., Aiyar, J., Hanson, D. C., Mather, R. J., Gutman, G. A., Karmilowicz, M. J., Auperin, D. D., and Chandy, K. G. (1994) *Mol. Pharmacol. 45*, 1227−1234.
9. Mullmann, T. J., Spence, K. T., Schroeder, N. E., Fremont, V., Christian, E. P., and Giangiacomo, K. M. (2001) *Biochemistry 40*, 10987−10997.
10. Bontems, F., Roumestand, C., Boyot, P., Gilquin, B., Doljansky, Y., Menez, A., and Toma, F. (1991) *Eur. J. Biochem. 196*, 19−28.
11. Johnson, B. A., and Sugg, E. E. (1992) *Biochemistry 31*, 8151−8159.
12. Dauplais, M., Gilquin, B., Possani, L. D., Gurrola-Briones, G., Roumestand, C., and Menez, A. (1995) *Biochemistry 34*, 16563−16573.
13. Johnson, B. A., Stevens, S. P., and Williamson, J. M. (1994) *Biochemistry 33*, 15061−15070.
14. Gairi, M., Romi, R., Fernandez, I., Rochat, H., Martin-Eauclaire, M. F., Van Rietschoten, J., Pons, M., and Giralt, E. (1997) *J. Pept. Sci. 3*, 314−319.
15. Krezel, A. M., Kasibhatla, C., Hidalgo, P., MacKinnon, R., and Wagner, G. (1995) *Protein Sci. 4*, 1478−1489.
16. Stampe, P., Kolmakova-Partensky, L., and Miller, C. (1994) *Biochemistry 33*, 443−450.
17. Marion, D., and Wuthrich, K. (1983) *Biochem. Biophys. Res. Commun. 113*, 967−974.
18. Piantini, U., Sorensen, O. W., and Ernst, R. R. (1982) *J. Am. Chem. Soc. 104*, 6800−6801.
19. Bax, A., and Davis, D. G. (1987) *J. Magn. Reson. 65*, 355−360.

20. Griesinger, C., Otting, G., Wuthrich, K., and Ernst, R. R. (1988) *J. Am. Chem. Soc. 110*, 7870−7872.
21. Jeener, J., Meier, B. H., Bachman, P., and Ernst, R. R. (1979) *J. Chem. Phys. 71*, 4546−4553.
22. Kumar, A., Ernst, R. R., and Wuthrich, K. (1981) *Biochem. Biophys. Res. Commun. 95*.
23. Piotto, M., Saudek, V., and Sklenar, V. (1992) *J. Biomol. NMR 2*, 661−665.
24. Eccles, C., and Guntert, P. (1991) *J. Biomol. NMR 1*, 111−130.
25. Wuthrich, K. (1986) *NMR of proteins and nucleic acids*, John Wiley, New York.
26. Guntert, P., Braun, W., and Wuthrich, K. (1991) *J. Mol. Biol. 217*, 517−530.
27. Guntert, P., and Wuthrich, K. (1991) *J. Biomol. NMR 1*, 447−456.
28. Brunger, A. T. (1992) *X-PLOR Version 3.1*, Yale University Press, New Haven, CT.
29. Roussel, A., and Cambillau, C. (1989) in *Silicon Graphics Geometry Partner Directory*, pp 77−78, Silicon Graphics, Mountain View, CA.
30. Koradi, R., and Billeter, M. (1996) *J. Mol. Graphics 14*, 51−55.
31. Laskowski, R. A., and Rullmann, J. A. (1996) *J. Biomol. NMR 8*, 477−486.
32. Nicholls, A., Sharp, K. A., and Honig, B. (1991) *Proteins 11*, 281−296.
33. Mullmann, T. J., Munujos, P., Garcia, M. L., and Giangiacomo, K. M. (1999) *Biochemistry 38*, 2395−2402.
34. MacKinnon, R., LaTorre, R., and Miller, C. (1989) *Biochemistry 28*, 8092−8099.
35. Park, C. S., and Miller, C. (1992) *Neuron 9*, 307−313.
36. Hidalgo, P., and MacKinnon, R. (1995) *Science 268*, 307−310.
37. Garcia, M. L., Garcia-Calvo, M., Hidalgo, P., Lee, A., and MacKinnon, R. (1994) *Biochemistry 33*, 6834−6839.
38. Bontems, F., Roumestand, C., Gilquin, B., Menez, A., and Toma, F. (1991) *Science 254*, 1521−1523.
39. Giangiacomo, K. M., Sugg, E. E., Garcia-Calvo, M., Leonard, R. J., McManus, O. B., Kaczorowski, G. J., and Garcia, M. L. (1993) *Biochemistry 32*, 2363−2370.
40. Doyle, D. A., Cabral, J. M., Pfuetzner, R. A., Kuo, A., Gulbis, J. M., Cohen, S. L., Chait, B. T., and MacKinnon, R. (1998) *Science 280*, 69−77.
41. Bontems, F., Gilquin, B., Roumestand, C., Menez, A., and Toma, F. (1992) *Biochemistry 31*, 7756−7764.

BI010228E